

Bi/Bi₂O₃/TiO₂ heterojunction photocathode for high-efficiency visible-light-driven lithium-sulfur batteries: Advancing light harvesting and polysulfide conversion

Shan Yi ^a, Zhe Su ^a, Hongli Chen ^a, Zhiqiang Zhao ^a, Xiaowei Wang ^a, Yayun Zhang ^a, Bo Niu ^{a,*}, Donghui Long ^{a,b,**}

^a Key Laboratory of Chemical Engineering, East China University of Science and Technology, Shanghai 200237, China

^b Key Laboratory for Specially Functional Materials and Related Technology of the Ministry of Education, East China University of Science and Technology, Shanghai 200237, China



ARTICLE INFO

Keywords:

Visible-light-driven
Li₂S₆-based photoelectrochemical lithium-sulfur batteries
Light harvesting
Polysulfide conversion
Photo-charging

ABSTRACT

Integrating solar-electrical energy conversion and electrical-chemical energy storage functions within a single device offers a promising strategy for efficient light harvesting, conversion, and storage of renewable solar energy. Herein, we develop visible-light-driven photoelectrochemical Li₂S₆-based lithium-sulfur batteries (VPLSBs) for simultaneous energy conversion and storage, employing a versatile Bi/Bi₂O₃/TiO₂ photocathode as both a light harvester and redox catalyst. The narrowed band gap of photocathode minimizes photoelectron-hole recombination, enabling efficient light-to-electrical energy conversion. Its energy level alignment with Li-S electrochemical potentials facilitates the photocarriers' participation in polysulfide conversions, supporting electrical-to-chemical energy storage. Under visible light, the Bi/Bi₂O₃/TiO₂ photocathode exhibits a photoelectrocatalysis effect, enhancing interfacial charge transfer, reducing Li₂S deposition resistance, and ensuring stable Li₂S plating/stripping. Additionally, the bare photo-charging process achieves an overall energy conversion-storage efficiency of 2.58 %. The VPLSB demonstrates an exceptional specific capacity of 1484 mA h g⁻¹ over 900 cycles, maintaining an apparent energy efficiency of 100.2 % at 0.2 mA cm⁻².

1. Introduction

Carbon-neutrality development paradigm is sparking a transformative shift in the energy landscape, seeking to address the challenges posed by climate change and reliance on fossil fuels by exploring alternative and renewable energy sources. Solar energy, in particular, holds significant promise as a clean and accessible resource, capable of meeting human energy needs with minimal emissions. However, the inherent intermittency and instability of solar energy resulting from day-night cycles pose challenges to its widespread adoption, leading to efforts focused on integrating continuous energy conversion and storage devices. Conventional solar energy utilization involves a two-stage process, starting with the conversion of solar energy into other forms, followed by energy storage [26]. Nonetheless, the hierarchical energy transfer and storage process may introduce energy dissipation and lead to significant efficiency degradation over extended cycles.

Lithium-sulfur (Li-S) batteries have gained significant attention in the realm of high-performance rechargeable devices, owing to their exceptional volumetric theoretical energy density (2835 Wh L⁻¹), high theoretical specific capacity (1675 mA h kg⁻¹), and cost-effective nature [17,22]. Whereas the complex chemical reactions between S₈ and Li₂S are a double-edged sword, as it both enables the high capacity of Li-S batteries and presents fatal challenges. The primary factors contributing to these challenges are the insulating properties of both S₈ and Li₂S, as well as the slow redox kinetics that lead to the dissolution of polysulfides. These issues can result in a severe shuttle effect, causing extra wasted sulfur, decreased battery capacity, and diminished cyclic performance. Fortunately, extensive research demonstrates the effectiveness of electrocatalytic materials in expediting the polysulfide transformation, particularly with the use of typical heterogeneous catalysts. Those heterogeneous catalysts facilitate the adsorption of polysulfides, enhance their conversion to lower-order species, promote

* Corresponding author.

** Corresponding author at: Key Laboratory of Chemical Engineering, East China University of Science and Technology, Shanghai 200237, China.

E-mail addresses: niubo@ecust.edu.cn (B. Niu), longdh@mail.ecust.edu.cn (D. Long).

efficient redox reactions, and mitigate the notorious shuttle effect, leading to improved performance and enhanced cycling stability of Li-S batteries.

The existing traditional two-stage utilization of solar energy, relying on grid-scale devices, faces limitations such as large system size and low energy density. And this unintegrated energy conversion-storage approach will inevitably cause huge losses of solar energy, hampering overall energy utilization efficiency [3,6,10]. Fortunately, the integration of photoactive electrodes into Li-S battery systems presents a promising avenue for achieving simultaneous light-electrical absorption and electrical-chemical energy storage, leading to highly efficient direct light-chemical-electrical energy conversion. In such photo-assisted Li-S batteries, the overall performance is influenced by two key factors: the photochemical activity of the photoelectrodes, which determines the light absorption efficiency, and the electrocatalytic capacity of the photoelectrodes, which governs the electrochemical energy storage effect [5,14,21]. By addressing these optimization aspects, the development of semiconductor electrodes with tailored band structures and precise potential alignment in photo-assisted Li-S batteries hold great promise for achieving direct and efficient light-electrical-chemical energy conversion and storage.

In this work, we develop visible-light-driven photoelectrochemical Li_2S_6 -based Li-S batteries with a $\text{Bi}/\text{Bi}_2\text{O}_3/\text{TiO}_2$ heterojunction cathode, which serves as a bifunctional light harvester and redox catalyst enabling efficient light-electrical-chemical energy conversion and storage. The light-permeable cell construction allows direct illumination of the cathode surface, promoting photochemical reactions and efficient energy conversion in Li_2S_6 -based batteries. The introduction of Bi_2O_3 enhances photocatalytic performance by forming a heterojunction with TiO_2 , leveraging its narrow bandgap for improved charge separation. Simultaneously, the incorporation of metallic Bi, with its semimetal properties, stimulates surface charges (SPR effect), ensuring high sensitivity and low recombination rates in sulfur conversion reactions. On the one side, the engineering of photoelectrode with a narrowed band gap can optimize the light-to-electrical conversion by suppressing photocarrier recombination and facilitating efficient charge separation and transfer (Fig. 1a). On the other side, its matched energy level with Li-S electrochemical potentials can realize the efficient catalysis of photocarriers to the polysulfide conversion process, thus promoting electrical-to-chemical energy storage (Fig. 1b) [20,40]. When exposed to visible light, the photoelectrocatalysis effect of the $\text{Bi}/\text{Bi}_2\text{O}_3/\text{TiO}_2$ photocathode leads to efficient interfacial charge transfer, the lower energy barrier for Li_2S deposition, and stable electrochemical plating/stripping of Li_2S . In addition, direct light-to-electrical conversion is achieved by the photovoltaic effect through the bare photo-charging

process, where absorbed light generates photoexcited electrons that flow through an external circuit, producing current and voltage (Fig. 1c and Fig. S1) [33]. As a result, the $\text{Bi}/\text{Bi}_2\text{O}_3/\text{TiO}_2$ VPLSB can release a photo-charging-stored capacity of $458.9 \text{ mA h g}^{-1}$ with a light energy utilization of 2.58 %. Even with more than 900 cycles, the $\text{Bi}/\text{Bi}_2\text{O}_3/\text{TiO}_2$ VPLSB can maintain a specific capacity of 1484 mA h g^{-1} with an apparent energy efficiency of 100.2 % at 0.2 mA cm^{-2} . This work presents a viable design of integrated visible-light-driven rechargeable batteries, offering a new approach towards achieving miniaturization, practicality, and long-term stability in solar energy storage.

2. Experimental Section

2.1. Materials

Carbon cloth was obtained from CeTech Co., Ltd. Tetrabutyl titanate ($\text{C}_{16}\text{H}_{36}\text{O}_4\text{Ti}$, AR), Titanium (IV) chloride (Cl_4Ti , 99.9 %), bismuth trinitrate ($\text{Bi}(\text{NO}_3)_3 \cdot 5\text{H}_2\text{O}$, 99.9 %), acetone (99.5 %), ethanol (99.8 %) were purchased from Macklin. Tetraethylene glycol dimethyl ether (TEGDME, 99 %), lithium sulfide (Li_2S , 99.98 %), sulfur powder, ethylene glycol (EG, GC), and hydrochloric acid (36–38 %) were purchased from Energy Chemical. The lithium anode and used LS-002 (1.0 M LiTFSI in DOL: DME = 1: 1 vol% with 1.0 % LiNO_3) electrolytes were purchased from MJS Corporation. The glass microfiber was purchased from Whatman (GF/A). The perforated coin cells were obtained from Guangdong Canrd New Energy Technology Co., Ltd.

2.2. Synthesis of TiO_2 coated carbon cloth

The carbon cloth ($4 \times 5 \text{ cm}^2$) was ultrasonically washed with acetone, ethanol, and deionized water (DI) three times, and dried at 60°C . The carbon cloth was dipped into a 0.2 M titanium (IV) chloride/DI solution under continuous magnetic stirring overnight, followed by being washed with DI water and dried at 60°C . Meanwhile, the homogenous hydrothermal solution consisting of tetrabutyl titanate (0.8 mL) and hydrochloric acid solution (40 mL, 6 M) was prepared, followed by adding the pretreated carbon cloth. After transferring into a 50 mL Teflon-lined autoclave, the solution was kept at 160°C for 4 h. Finally, the as-formed carbon cloth was washed with DI water several times and dried under 60°C to obtain the TiO_2 coated carbon cloth.

2.3. Synthesis of the $\text{Bi}/\text{Bi}_2\text{O}_3/\text{TiO}_2$ coated carbon cloth

First, the mixed solution of 500 mg bismuth trinitrate and 12 mL EG was magnetically stirred for 30 min. Following the addition of 24 mL

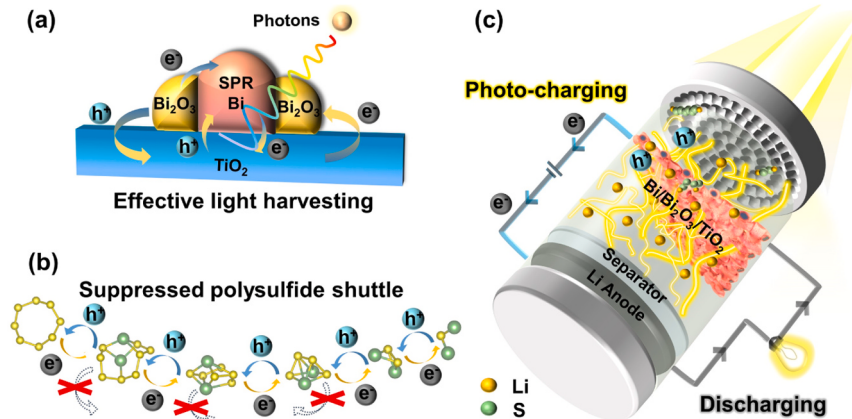


Fig. 1. (a) Illustration of the generation and transfer of the photoelectron-hole pairs upon visible light absorption in the $\text{Bi}/\text{Bi}_2\text{O}_3/\text{TiO}_2$ photocathode. (b) Schematic illustration of photogenerated electron-hole pairs promoting polysulfide conversion and suppressing shuttling effect. (c) Illustration of the direct light-to-electrical phenomenon in $\text{Bi}/\text{Bi}_2\text{O}_3/\text{TiO}_2$ VPLSBs during the bare photo-charging process.

ethanol, the solution was kept under ultrasonic conditions for 30 min and then stirred for 30 min to obtain solvothermal solution A. TiO_2 coated carbon cloth was then impregnated in the solution for 6 hours and removed to dry at 70 °C for 10 min and 300 °C for 5 min. After adding the dried carbon cloth, the former solution A was transferred to a Teflon-lined autoclave and kept at 160 °C for 5 hours. And the as-formed carbon cloth was cleared by DI and ethanol repeatedly, followed by a six-hour vacuum freeze drying under –90 °C. Finally, the $\text{Bi}/\text{Bi}_2\text{O}_3/\text{TiO}_2$ coated carbon cloth was obtained after annealing at 600 °C for 2 h in an Argon atmosphere at a rate of 3 °C min⁻¹. Here, the amount of $\text{Bi}/\text{Bi}_2\text{O}_3/\text{TiO}_2$ is ca. 5.6 mg cm⁻².

2.4. Synthesis of Bi_2O_3 coated carbon cloth

The procedure of constructing Bi_2O_3 coated carbon cloth is similar to that of $\text{Bi}/\text{Bi}_2\text{O}_3/\text{TiO}_2$ coated carbon cloth, with the exception that the step of growing titanium dioxide is omitted. Specifically, the carbon cloth (4*5 cm²) was ultrasonically washed with acetone, ethanol, and deionized water (DI) three times, and dried at 60 °C. The mixed solution of 500 mg bismuth trinitrate and 12 mL EG was magnetically stirred for 30 min. Following the addition of 24 mL ethanol, the solution was kept under ultrasonic conditions for 30 min and then stirred for 30 min to obtain solvothermal solution A. The pure carbon cloth was then impregnated in the solution for 6 hours and removed to dry at 70 °C for 10 min and 300 °C for 5 min. After adding the dried carbon cloth, the former solution A was transferred to a Teflon-lined autoclave and kept at 160 °C for 5 hours. And the as-formed carbon cloth was cleared by DI and ethanol repeatedly, followed by a six-hour vacuum freeze drying under –90 °C. Finally, the $\text{Bi}/\text{Bi}_2\text{O}_3/\text{TiO}_2$ coated carbon cloth was obtained after annealing at 600 °C for 2 h in an Argon atmosphere at a rate of 3 °C min⁻¹.

2.5. Characterization

The surficial chemical composition was detected using the Raman spectra (HORIBA Scientific LabRAM HR Evolution), X-ray photoelectron spectrometer (XPS, Thermo Scientific K-Alpha⁺), X-ray diffraction (XRD, Bruker D8 advance) with Cu K α radiation ($\lambda = 1.5406 \text{ \AA}$) at a scan rate of 5° min⁻¹ between 5° and 90° under 40 KV voltage. The microstructures and morphologies of $\text{Bi}/\text{Bi}_2\text{O}_3/\text{TiO}_2$ were investigated by field emission scanning electron microscopy (FESEM, JEOL 7100F) and transmission electron microscopy (TEM, JEOL 2100F). The elemental distributions and line-scan profiles of $\text{Bi}/\text{Bi}_2\text{O}_3/\text{TiO}_2$ were analyzed by using energy dispersive spectroscopy (EDS) affiliated with the TEM (JEOL 2100F). Photoluminescence emission spectroscopy (PL) of various samples was collected by FLS1000 spectrophotometer. An ultraviolet-visible (UV-vis) spectrophotometer (Shimadzu UV-3600) was utilized to identify the absorption spectra of various samples, and the linear relationship between the absorption coefficient and the optical band gap is,

$$\frac{\alpha h v}{m} = B(h v - E_g) \quad (1)$$

Here, α , h , v refer to the molar absorption coefficient, the Planck constant ($4.1356676969 \text{ E}^{-15} \text{ eV s}^{-1}$), and the incident photon frequency. The magnitude of m is contingent upon the material of the semiconductor and the corresponding transition type. B can be treated as a proportionality constant, and E_g denotes the optical band gap of a semiconductor material. In-situ optical observation of the deposition behavior in the $\text{Bi}/\text{Bi}_2\text{O}_3/\text{TiO}_2$ VPLSBs was conducted through an optical cell and recorded by a microscope (YM710R).

2.6. Assembling of light-permeable coin cell and air-tight in-situ cell

Electrochemical performances were inspected by using perforated 2032-type coin cells. To ensure adequate light transmission, 0.7 mm

diameter holes are arranged within a 12 mm diameter circle, and a transparent PET film and a UV-curing adhesive are applied to seal the exterior of the light-transmitting window to enhance airtightness. A Xe lamp (500 W) was selected as the light source with a 350–780 nm cutoff filter (VisREF), and the luminous power was calibrated to be 0.06 W cm⁻² for all tests. The anode and separator are lithium foil and glass fiber, and the $\text{Bi}/\text{Bi}_2\text{O}_3/\text{TiO}_2$ (1*1 cm²) is used as the cathode. The selection of glass fiber membrane material, characterized by its high pore size and porosity, ensures the feasibility and stability of a high electrolyte quantity. 0.4 M Li_2S_6 solution was prepared by uniformly mixing sublimation sulfur and Li_2S into the LS-002 electrolyte at 60 °C in a molar ratio of 5:1. The electrolyte dosage for each cell was set at 13 μL mg⁻¹, allowing the calculation of the actual doping amount of Li_2S_6 -contained electrolyte. Thus, the areal mass loading of sulfur in the cathode is calculated to be 9.236 mg cm⁻². And the N/P value can be determined to be 1.105. An air-tight in-situ cell was assembled using an electrolyte consisting of 0.1 M Li_2S_6 in 1 M LiTFSI/DME/DOL solution with 0.1 M LiNO_3 . The $\text{Bi}/\text{Bi}_2\text{O}_3/\text{TiO}_2$ film serves as the working electrode, a two-millimeter non-conductive ring mold as the separation layer, and a one-hundred-micron lithium foil as the counter/reference electrode.

2.7. Electrochemical measurements

Electrochemical impedance spectroscopy (EIS) and cyclic voltammetry (CV) experiments were conducted on the Biologic potentiostat within a scan frequency range from 1 MHz to 0.01 Hz and a scan rate from 0.1 to 2 mV s⁻¹. The cycling performances of the $\text{Bi}/\text{Bi}_2\text{O}_3/\text{TiO}_2$ VPLSBs were evaluated between 1.7 and 2.8 V (vs. Li/Li⁺) on the standard multi-channel Land CT 2001A and Neware CT-4000 battery testing systems. The transient photocurrent response, Mott-Schottky curves, and Tafel plots were measured in a three-electrode configuration and recorded by a CHI 660E electrochemical workstation, in which the 0.4 M Li_2S_6 solution was used as electrolyte.

2.8. Li_2S precipitation tests

0.25 M Li_2S_8 electrolyte was prepared by uniformly mixing Li_2S and sublimation sulfur powders in a moral ratio of 7:1 into TEGDME solvent at room temperature in the glovebox. The $\text{Bi}/\text{Bi}_2\text{O}_3/\text{TiO}_2$, glass fiber, and lithium foil were used as the cathode, separator, and anode. the cathode side and anode side were applied with 20 μL LS002 electrolyte and 20 μL Li_2S_8 electrolyte with a volume ratio of 1:1, respectively. The precipitation process was initiated by discharging the assembled cells galvanostatically at 0.112 μA until the voltage dropped below 2.06 V, then discharging them potentiostatically at 2.05 V until the response current was less than 0.01 mA.

2.9. Polysulfide adsorption test

A 5 mM Li_2S_6 solution was acquired by combining Li_2S and S in a molar ratio of 1:5 in the DME/DOL solvent (volume ratio of 1:1) while subject to magnetic stirring at 60°C for 24 hours. Subsequently, four 1 cm² carbon cloth (CC), $\text{Bi}/\text{Bi}_2\text{O}_3/\text{TiO}_2$ -CC and TiO_2 -CC were immersed in the 5 mM Li_2S_6 solution for visualized adsorption test. Ex-situ ultraviolet-visible (UV) absorption spectra and XPS spectra were measured after the samples had been soaked in the Li_2S_6 solution for 12 hours. All these procedures were conducted within an argon-filled glove box.

2.10. Method of DFT calculations

All the theoretical calculations were carried out with the density functional theory (DFT) method as implemented in the Vienna Ab Initio Simulation Package (VASP).^[18] The electron-ion interaction was described with the projector augmented wave (PAW) method,^[1] while the electron exchange and correlation energy were solved within the generalized gradient approximation with the Perdew-Burke-Ernzerhof

(PBE) exchange-correlation functional.[29,30] The kinetic energy cutoff of the plane wave was set to be 500 eV and the convergence criterion for the residual forces and total energies were set to be 0.03 eV Å⁻¹ and 10⁻⁵ eV, respectively. The positions of the conduction band (CB) and valence band (VB) of Bi₂O₃ at the point of zero charges were predicted theoretically by the following empirical equations:

$$E_{\text{CB}} = X - E^C - 0.5E_g \quad (2)$$

$$E_{\text{VB}} = E_{\text{CB}} + E_g \quad (3)$$

where E_{CB} and E_{VB} are the potentials of the conduction band and valence band, respectively; X is the absolute electronegativity of the semiconductor, which is defined as the geometric mean of the absolute electronegativity of the constituent atoms; The X value of Bi₂O₃ is 5.986 eV.[8] E^C is the energy of free electrons on the hydrogen scale (ca. 4.44 eV), and E_g is the band gap of the semiconductor.

3. Results and discussion

The synthesis of the Bi/Bi₂O₃/TiO₂ coated carbon cloth involves a hydrothermal formation of TiO₂ nanorods on the carbon fiber, followed by the solvothermal introduction of Bi/Bi₂O₃ onto the TiO₂ nanorods, and final annealing at 600 °C in an Argon atmosphere (Fig. 2a). The obtained Bi/Bi₂O₃/TiO₂ composite exhibits a visually distinct light gray appearance, with the Bi/Bi₂O₃/TiO₂ content estimated at around 27.22 % through thermogravimetric analysis (Fig. S2). The original carbon cloth substrate has a flat woven surface with a fiber diameter of

approximately 10 µm (Fig. S3). In the synthesis process, Bi₂O₃ displays a melon-like growth morphology on the surface of carbon fibers (Fig. S4a-b), while slender TiO₂ nanorods grow in a well-aligned configuration on the carbon fiber (Fig. S4c-d). Upon comparison between the prepared Bi/Bi₂O₃/TiO₂ coated carbon fiber (Fig. 2b-c and Fig. S4e-f) and the pristine TiO₂ coated carbon fiber (Fig. S4g-h), it is evident that the subsequent introduction of Bi/Bi₂O₃ effectively envelopes the surface of the TiO₂ nanorods without causing significant alterations to the overall morphology. The uniform spatial distribution of the Bi, Ti, and O elements can be revealed by the element mappings of the Bi/Bi₂O₃/TiO₂ coated carbon fiber (Fig. S5). TEM image shows that the Bi/Bi₂O₃ decorates the surface of individual TiO₂ nanorods with a size of 5–8 nm (Fig. 2d). Further examination through HRTEM images and SEAD pattern analysis confirms the presence of crystal planes corresponding to TiO₂ (110), Bi₂O₃ (111), and Bi (012) in the Bi/Bi₂O₃/TiO₂ composite (Fig. 2e). Additionally, the HAADF line-scan intensity profile demonstrates the formation of TiO₂ nanorods with the surficial decoration of Bi and Bi₂O₃ (Fig. 2f). And the elemental mapping images from the nanoscale level further reveal the uniform distribution of the Bi and Bi₂O₃ particles on the individual TiO₂ nanorod (Fig. 2g). These findings confirm the successful preparation of the Bi/Bi₂O₃/TiO₂ heterostructure.

The crystalline phases of the Bi/Bi₂O₃/TiO₂ heterostructure are investigated using the XRD pattern, as shown in Fig. 3a. Rutile phase TiO₂ (JCPDS No. 87-0710) can be clearly observed, known for its exceptional light-trapping, photocatalytic properties, and efficient photo-carrier separation and transport.[38] Additionally, the XRD

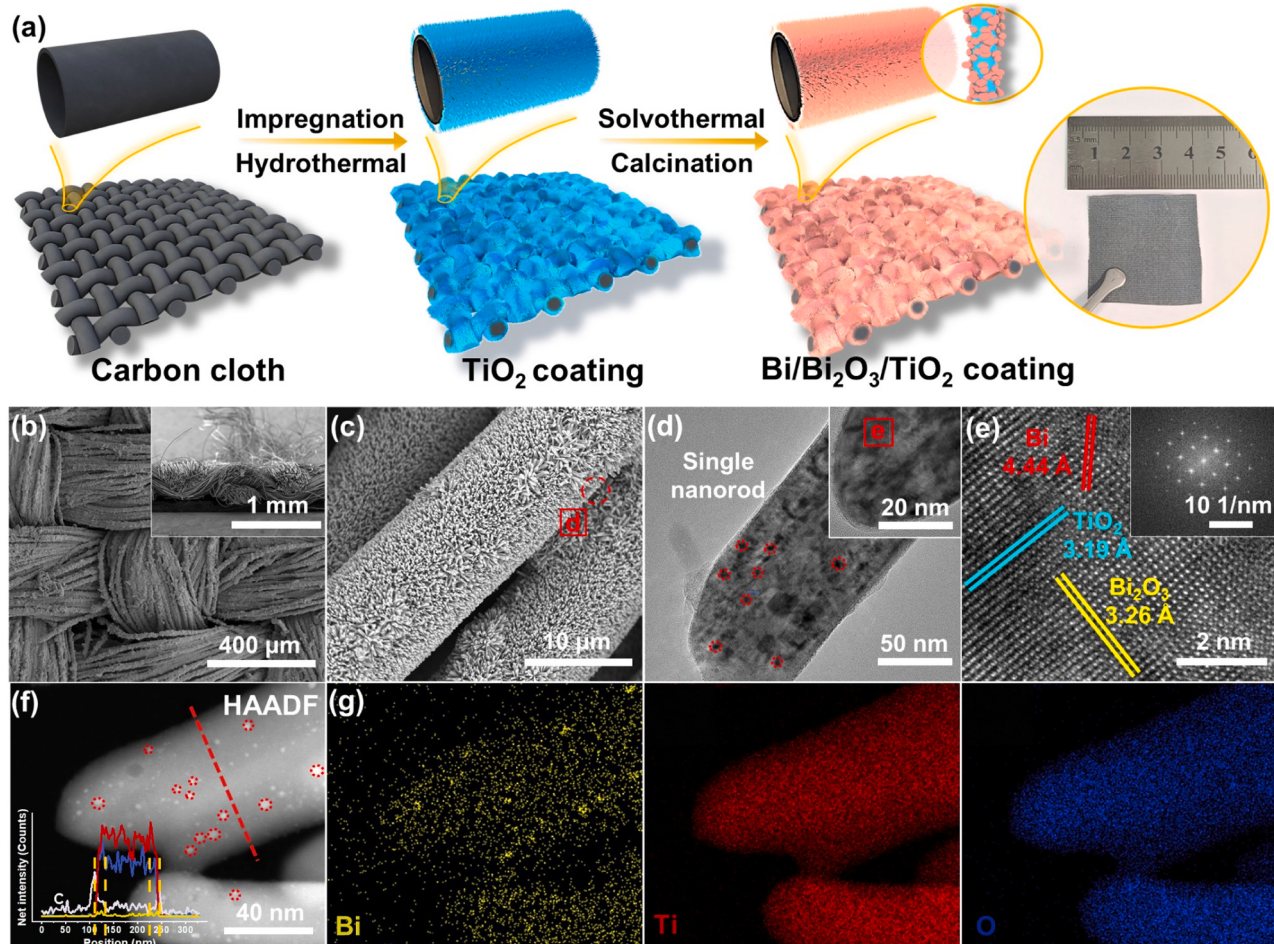


Fig. 2. (a) Schematic illustration of the formation of the Bi/Bi₂O₃/TiO₂ on carbon cloth. (b, c) Top-view and cross-section SEM images, (d) TEM image of the Bi/Bi₂O₃/TiO₂ on carbon cloth. (e) HRTEM images and corresponding SEAD pattern of the Bi/Bi₂O₃/TiO₂ heterostructure. (f) HAADF-STEM image with line-scan profile and (g) elemental mapping images of an individual Bi/Bi₂O₃ coated TiO₂ nanorod.

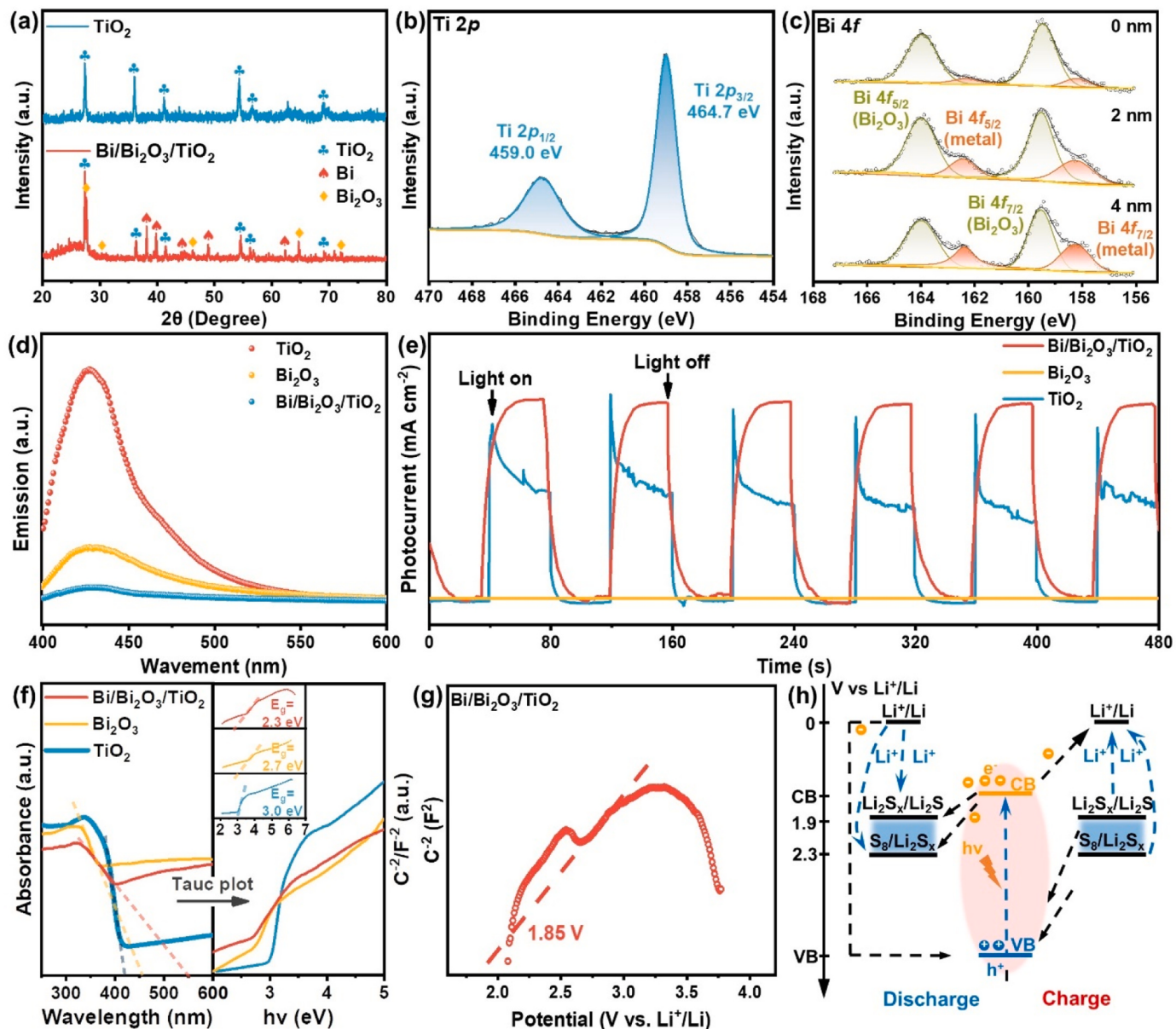


Fig. 3. (a) XRD patterns of the $\text{Bi}/\text{Bi}_2\text{O}_3/\text{TiO}_2$. (b) High-resolution XPS spectrum of $\text{Ti} 2p$ of the $\text{Bi}/\text{Bi}_2\text{O}_3/\text{TiO}_2$. (c) XPS depth profiling spectra of the Bi element in $\text{Bi}/\text{Bi}_2\text{O}_3/\text{TiO}_2$ at different etching depths (0, 2, 4 nm). (d) Photoluminescence emission spectra, (e) transient photocurrent response plots under a light intensity of 0.02 W cm^{-2} , (f) UV-vis spectra with the resultant Tauc plots, and (g) Mott-Schottky curves of the TiO_2 , Bi_2O_3 , and $\text{Bi}/\text{Bi}_2\text{O}_3/\text{TiO}_2$. (h) Energy diagram of $\text{Bi}/\text{Bi}_2\text{O}_3/\text{TiO}_2$ and $\text{Li}_2\text{S}/\text{S}_8$ vs. Li^+/Li .

patterns of the composite $\text{Bi}/\text{Bi}_2\text{O}_3/\text{TiO}_2$ present narrow and sharp peaks index to the hexagonal Bi (JCPDS No. 85-1331) and Bi_2O_3 (JCPDS No. 52-1007), indicating their good crystallinity. XPS analysis confirms the presence of Bi, Ti, O, and C elements, with corresponding contents of 1.11 wt%, 13.77 %, 44.15 %, and 40.97 % (Fig. S6 and Table S1). In the $\text{Ti} 2p$ spectrum, signals at 459.0 and 464.7 eV are attributed to $\text{Ti}^{4+} 2p_{1/2}$ and $\text{Ti}^{4+} 2p_{3/2}$ of the TiO_2 , respectively (Fig. 3b). The Bi 4f spectrum reveals two pairs of peaks at 157.6/162.4 eV and 159.1/164.3 eV, corresponding to metallic Bi^0 and Bi^{3+} states, respectively (Fig. 3c). Meanwhile, the coexistence relationship of the Bi_2O_3 coating layer around Bi is investigated using XPS sputter depth profiling techniques (Fig. S7), which reveals an increased Bi^0 peak strength and a decreased Bi^{3+} peak strength with increasing etching depth. Furthermore, the heterostructure of $\text{Bi}/\text{Bi}_2\text{O}_3/\text{TiO}_2$ is demonstrated by XPS peak displacements compared to pure Bi_2O_3 and TiO_2 samples (Fig. S8-9). The Bi characteristic peak in $\text{Bi}/\text{Bi}_2\text{O}_3/\text{TiO}_2$ shifts towards lower energies,

indicating an increase in electron density around the Bi atom, potentially due to the capturing of surrounding electrons in the heterostructure.[9] Moreover, the binding energies of $\text{Ti} 2p_{3/2}$ and $2p_{1/2}$ peaks in $\text{Bi}/\text{Bi}_2\text{O}_3/\text{TiO}_2$ are higher than in pure TiO_2 , suggesting a relatively weak electron affinity caused by partial electron loss during the formation of the heterostructure.

To evaluate the light-to-chemical capability of the $\text{Bi}/\text{Bi}_2\text{O}_3/\text{TiO}_2$ material as a photocathode, the photoelectric activity is characterized. The pure TiO_2 and Bi_2O_3 coated carbon cloth is prepared in the same technology and annealed at the same 600°C for comparison. In the photoluminescence (PL) spectroscopy tests, the $\text{Bi}/\text{Bi}_2\text{O}_3/\text{TiO}_2$ has the lowest emission band area in contrast to Bi_2O_3 and TiO_2 samples among a range from 400 to 500 nm, indicating the suppressed photogenerated carrier recombination (Fig. 3d). The direct transient photocurrent response tests are also compared between $\text{Bi}/\text{Bi}_2\text{O}_3/\text{TiO}_2$, Bi_2O_3 , and TiO_2 samples in Fig. 3e, by applying alternating 40-second light and

dark conditions. Upon exposure to visible light, the $\text{Bi}/\text{Bi}_2\text{O}_3/\text{TiO}_2$ exhibits a quick-balanced, potent, and steady photo-response plot within three-electrode system under a light intensity of 0.02 W cm^{-2} . Even under higher light intensities, the $\text{Bi}/\text{Bi}_2\text{O}_3/\text{TiO}_2$ photoelectrode can also maintain a fast and sensitive photo-response current (Fig. S10). By contrast, the TiO_2 has an initial surge in current followed by a significant decline while Bi_2O_3 has almost unresponsive. The incorporation of semi-metallic Bi facilitates the generation of high-sensitivity, low-recombination paired photogenerated carriers, capitalizing on advantages such as bandgap adjustment, SPR effects, protective layers, and charge transfer bridges. These attributes are essential for ensuring the efficiency of photocatalytic sulfur conversion. As a criterion of the light-harvesting potential, the optical bandgap properties of the $\text{Bi}/\text{Bi}_2\text{O}_3/\text{TiO}_2$ as a semiconductor is further investigated by ultraviolet-visible (UV-vis) spectra. The optical band gap energies can be determined by applying the TAUC plot method to UV-vis absorbance measurement with the equation: $(ah\nu)^{1/m} = B(h\nu - E_g)$. Clearly, the $\text{Bi}/\text{Bi}_2\text{O}_3/\text{TiO}_2$ composite, with a lower bandgap of 2.3 eV , has extended its absorption edge to 550 nm compared to Bi_2O_3 ($456 \text{ nm}, 2.7 \text{ eV}$) and TiO_2 ($419 \text{ nm}, 3.0 \text{ eV}$). This expansion has significantly enhanced its ability to absorb visible light (Fig. 3f). The excellent photoelectric activity of $\text{Bi}/\text{Bi}_2\text{O}_3/\text{TiO}_2$ heterostructure leads to abundant and persistent photocarriers at the interface under visible light, as evidenced by reduced contact impedance and charge-transfer impedance compared to Bi_2O_3 and TiO_2 (Fig. S11).

The electronic structure of the $\text{Bi}/\text{Bi}_2\text{O}_3/\text{TiO}_2$ heterostructure is explored using Mott-Schottky (M-S) analysis. The positive slope can be observed in the plotted M-S curve in Fig. 3g, indicating the n-type

semiconductor behavior of the $\text{Bi}/\text{Bi}_2\text{O}_3/\text{TiO}_2$ heterojunction, with electrons being the primary carriers. The flat band potential (E_{FB}) value is determined to be 1.85 V (vs. Li^+/Li), obtained from the proportional intercept with the horizontal axis. And the valence band (E_{VB}) and E_{CB} of $\text{Bi}/\text{Bi}_2\text{O}_3/\text{TiO}_2$ can be estimated to be 4.04 V and 1.75 V (vs. Li^+/Li), as it is typical of n-type semiconductors to possess a conduction band (E_{CB}) approximately 0.1 V lower than Fermi level (E_{FB}) [35]. Furthermore, the voltage range of $1.9\text{--}2.3 \text{ V}$ represents the entire electrochemical reaction of the Li-S system, consisting of polysulfides conversion and Li_2S deposits process. The resulting energy band diagram of $\text{Bi}/\text{Bi}_2\text{O}_3/\text{TiO}_2$ is exhibited in Fig. 3h, which shows the adequate covers upon the Li-S redox potential range. Such matched energy levels between photocathode and redox reactions can guarantee the production, transportation, and injection of photoelectrons/holes, thus participating in and promoting the polysulfide conversion process.

To investigate the photoelectrocatalysis effect of the $\text{Bi}/\text{Bi}_2\text{O}_3/\text{TiO}_2$ photocathode in a visible-light-driven battery system, the comparative analysis of the electrochemical performance is conducted under both visible light and dark conditions at an external voltage of $1.7\text{--}2.8 \text{ V}$. In order to ensure accurate results, several measures are taken. Firstly, visible-light-driven photoelectrochemical batteries (VPLSBs) are developed, where the cathode case is sealed with transparent PET tape and UV curing adhesive to ensure light-permeability and air-tightness (Fig. S12). This allows for direct irradiation of the electrode by visible light. Secondly, the electrolyte dosage is carefully controlled to maintain consistent conditions during testing. Lastly, to minimize the influence of light intensity from the source, an intensity of 0.06 W cm^{-2} was

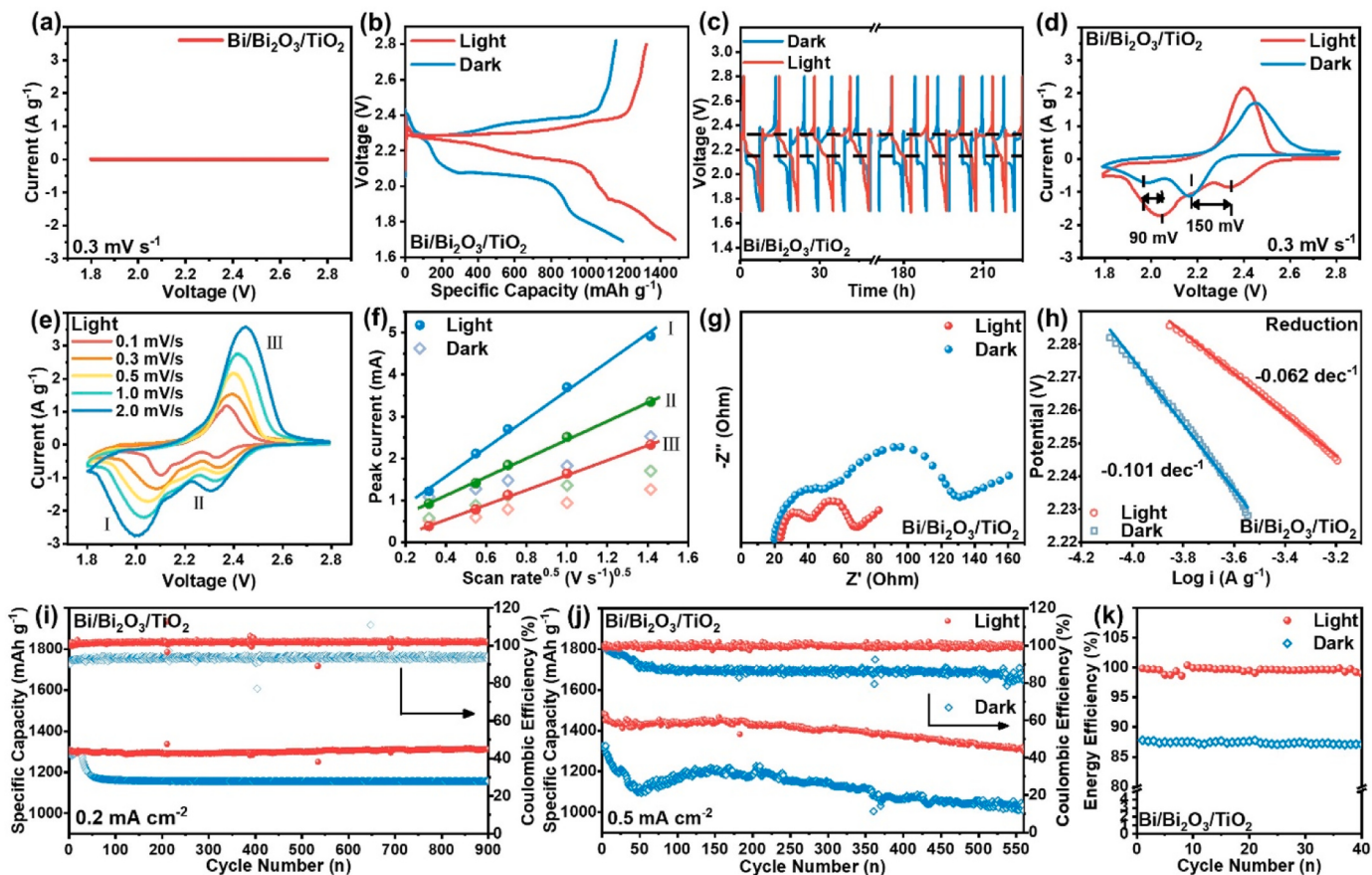


Fig. 4. (a) CV spectra at a scan rate of 0.3 mV s^{-1} of $\text{Bi}/\text{Bi}_2\text{O}_3/\text{TiO}_2$ Li-metal battery without the addition of Li_2S_6 electrolyte under dark conditions. (b) Initial-cycle and (c) long-term GDC curves of $\text{Bi}/\text{Bi}_2\text{O}_3/\text{TiO}_2$ VPLSBs under visible light at 0.5 mA cm^{-2} . (d) CV spectra at a scan rate of 0.3 mV s^{-1} of the $\text{Bi}/\text{Bi}_2\text{O}_3/\text{TiO}_2$ VPLSBs with and without visible light. (e) CV spectra at a scan rate of 0.3 mV s^{-1} and (f) plots of CV peak currents vs. the square root of the scan rate under visible light. (g) Electrochemical impedance spectra (EIS) and (h) Tafel plots of $\text{Bi}/\text{Bi}_2\text{O}_3/\text{TiO}_2$ VPLSBs under dark and light conditions. Long-term GDC cycling performances of the $\text{Bi}/\text{Bi}_2\text{O}_3/\text{TiO}_2$ VPLSBs with and without visible light at (i) 0.2 mA cm^{-2} , (j) 0.5 mA cm^{-2} with (k) energy efficiencies.

maintained, and the VisREF filter (350–780 nm) as well as the air convection circulation device were used to reduce the impact of heat energy on battery performance (Fig. S13). These precautions ensure that the electrochemical tests accurately reflect the performance of the Bi/Bi₂O₃/TiO₂ photocathode under visible light conditions and provide valuable insights into its photocatalytic capabilities in the battery system.

Specifically, the Bi/Bi₂O₃/TiO₂ exhibits negligible redox capability in the chosen ether-based electrolyte system, as evidenced in Fig. 4a, where CV spectra show no discernible current without Li₂S₆ electrolyte under dark conditions. A visual adsorption experiment for polysulfides confirms the enhanced adsorption capability of Bi/Bi₂O₃/TiO₂-loaded carbon cloth, evidenced by a pale yellow, transparent solution after 12 h, contrasting with minimal color change in pure carbon cloth solution (Figure S14(a)). UV-visible absorption spectroscopy (Figure S14(b)) further supports this, showing weaker absorption for Bi/Bi₂O₃/TiO₂ compared to the original Li₂S₆ solution, suggesting stronger adsorption. XPS analysis of Bi 4f spectrum displayed a slight upward shift after absorption (Figure S14(c)), suggesting bond formation between Bi and S, reaffirming Bi/Bi₂O₃/TiO₂'s effective adsorption for LiPSs and offering insights into the adsorption mechanism.

The consistent composition and proportion of the Bi in the Bi/Bi₂O₃/TiO₂ at different voltages at the 50th cycles are revealed by XPS spectra, providing compelling evidence for the enduring stability within photo-electrode over extended periods (Fig. S15). While in the Li-S battery system, the galvanostatic discharge/charge (GDC) tests at 0.5 mA cm⁻² reveal a significantly lower overpotential under light illumination compared to dark conditions (Fig. 4b and Fig. S16). In particular, this advantageous interfacial resistance remains stable over 230 hours under visible light (Fig. 4c and Fig. S17). Even when subjected to varying rates, light exposure ensures that Bi/Bi₂O₃/TiO₂ VPLSBs maintain a charge-discharge plateau without significant overpotential (Fig. S18(a)), indicating enhanced electrochemical kinetic performance throughout the entire reaction process. Consequently, these batteries exhibit superior high-capacity retention and high reversibility rate performance under light conditions, with average discharge capacities at 0.2, 0.5, 1, and 2 C being 1472.6, 1334.3, 1189.1, and 1087.0 mA h g⁻¹, respectively. These values far exceed the corresponding capacities in the dark, which are 1095.1, 988.2, 873.0, and 642.8 mA h g⁻¹ (Fig. S18(b)). Cyclic voltammograms (CV) confirm the conventional redox reaction path at 0.3 mV s⁻¹, with intensified response currents and positive shifts of 90 mV and 150 mV in anodic oxidation peaks under visible light (Fig. 4d). These effects can be attributed to the photoelectrocatalysis of the Bi/Bi₂O₃/TiO₂ photocathode that promotes conversion between soluble polysulfides and insoluble Li₂S₂/Li₂S and S₈. The lower overpotentials and higher current response are well maintained under visible light even at different scan rates (Fig. 4e and Fig. S19). Enhanced light intensity leads to the transformation of oxidation peaks from single to dual, accompanied by shifts to lower onset and peak voltages in the sulfur oxidation process, signifying improved electrochemical kinetics and an overall promoted photocatalytic effect (Fig. S20). Quantitatively, the Randles-Sevcik equation shows better linearity and higher fitting slope in light-illuminated Bi/Bi₂O₃/TiO₂ VPLSBs, suggesting its enhanced species mobility and diffusivity (Fig. 4f and Equation S1). Moreover, EIS results show smaller high and medium-frequency semi-circles in Nyquist plots under visible light, indicating its improved interfacial resistance and species transportation (Fig. 4g). While Tafel plots exhibit decreased slopes under light conditions (0.163/−0.062 V dec⁻¹) compared to dark conditions (0.199/−0.101 V dec⁻¹), implying its enhanced oxidation/reduction processes (Fig. 4h and Fig. S21). The significantly improved interface polarization and transfer efficiency in the Bi/Bi₂O₃/TiO₂ photocathode can be attributed to its photoelectrocatalysis effect, which facilitates the stable generation of abundant photocarriers, leading to efficient charge distribution on the interface.

The impact of visible light on the long-term cycling performance of

the Bi/Bi₂O₃/TiO₂ VPLSBs is further evaluated. At a current density of 0.2 mA cm⁻², the long-term GDC curve of the Bi/Bi₂O₃/TiO₂ VPLSB shows a reversible coulomb efficiency of 100.2 % over 900 cycles under visible light, implying the input of additional capacity (Fig. 4i). This behavior can be attributed to the efficient conversion of photogenerated electrons into electricity through the photovoltaic effect, resulting from the photoexcitation of the Bi/Bi₂O₃/TiO₂ photocathode under visible light. Even when the current density rises to 0.5 mA cm⁻², the light-illuminated Bi/Bi₂O₃/TiO₂ VPLSB presents a larger initial specific capacity under visible light (1487 mA h g⁻¹) than dark conditions (1315 mA h g⁻¹), corresponding to a 13 % increase in sulfur utilization. Remarkably, during a prolonged period of 560 cycles, the light-illuminated Bi/Bi₂O₃/TiO₂ VPLSB has a high specific capacity of 1320 mA h g⁻¹ with a Coulombic efficiency of over 100 %, whereas dark conditions lead to a continuously declining capacity (Fig. 4j). The reduction in capacity observed during extended cycling at high current density might be attributed to the intricate interplay of various factors, including the growth of lithium dendrites, alterations in electrolyte electrochemical stability, interfacial electrochemical reactions, side reactions, and material loss. Given that the overall energy efficiency (OEE) is a crucial index of all photovoltaic technologies, the EE of the Bi/Bi₂O₃/TiO₂ VPLSBs at 0.5 mA cm⁻² is evaluated for assessment of visible light utilization efficiency. The OEE value can be determined using the equation above,

$$\eta_{\text{conversion}} = E_{\text{discharge}} / E_{\text{charge}} \times 100\% \quad (1)$$

where $E_{\text{discharge}}$ and E_{charge} denote the apparent discharged voltage and the total input charged voltage of the batteries. Obviously, the presence of visible light maintains the OEE efficiency of the VPLSB above 100 %, indicating an apparent lossless energy conversion process. While the absence of light leads to a significantly low energy efficiency of 87.5 %, implying an eighth of the energy loss during the round-trip conversion processes (Fig. 4k). Even under more practical low E/S conditions (6 and 10 μL mg⁻¹), the Bi/Bi₂O₃/TiO₂ VPLSBs maintain remarkably high Coulombic efficiency and outstanding capacity retention under illumination, far exceeding the continuously decreasing Coulombic efficiency and capacity of the battery in dark conditions (Fig. S22). The superior performance of the Bi/Bi₂O₃/TiO₂ photocathode in the Li-S battery system is achieved through the synergistic effects of promoting the sulfur redox process via photoelectrocatalysis and harnessing additional energy from the photovoltaic effect.

To investigate the influence of visible light on Li₂S nucleation and growth behavior in the Bi/Bi₂O₃/TiO₂ VPLSB, potentiostatic Li₂S precipitation tests are conducted in the Li₂S₈ electrolyte system (Fig. 5a-b). Visible light exposure leads to a larger Li₂S precipitation capacity of 429.6 mA h g⁻¹ and a shorter peak current time (1900 s) compared to dark conditions (222.8 mA h g⁻¹, 6000 s), indicating its higher reactivity and faster electrochemical response. Furthermore, the Li₂S deposition model is assessed by dimensionless I-t transient plots (Fig. 5c) fitted to the Scharifker-Hills model (Equation S2-5). [31] Light exposure is found to guide accelerated nucleation rates dominated by ion diffusion in the VPLSB, with hybrid nucleation patterns observed for the three-dimensional instantaneous (3DI) and progressive (3DP) models. While dark conditions lead to a hybrid of two-dimensional instantaneous (2DI) and 3DP models, suggesting a constrained nucleation rate influenced by both ion diffusion and lattice incorporation. SEM images confirm the favorable deposition morphology under light, with 3D Li₂S nucleation along nanorods and regular filling of porous matrix void spaces, while dark conditions result in disorderly deposition with dendritic structures and sheet-like coverings (Fig. 5d-f). Even after the 50th cycle, when fully charged, the presence of visible light preserves the structural integrity and surface uniformity of the Bi/Bi₂O₃/TiO₂ photocathode, which stands in stark contrast to the significant coverage of inactive substances observed without light illumination (Fig. S23). In-situ optical monitoring is further applied by an in-situ optical device

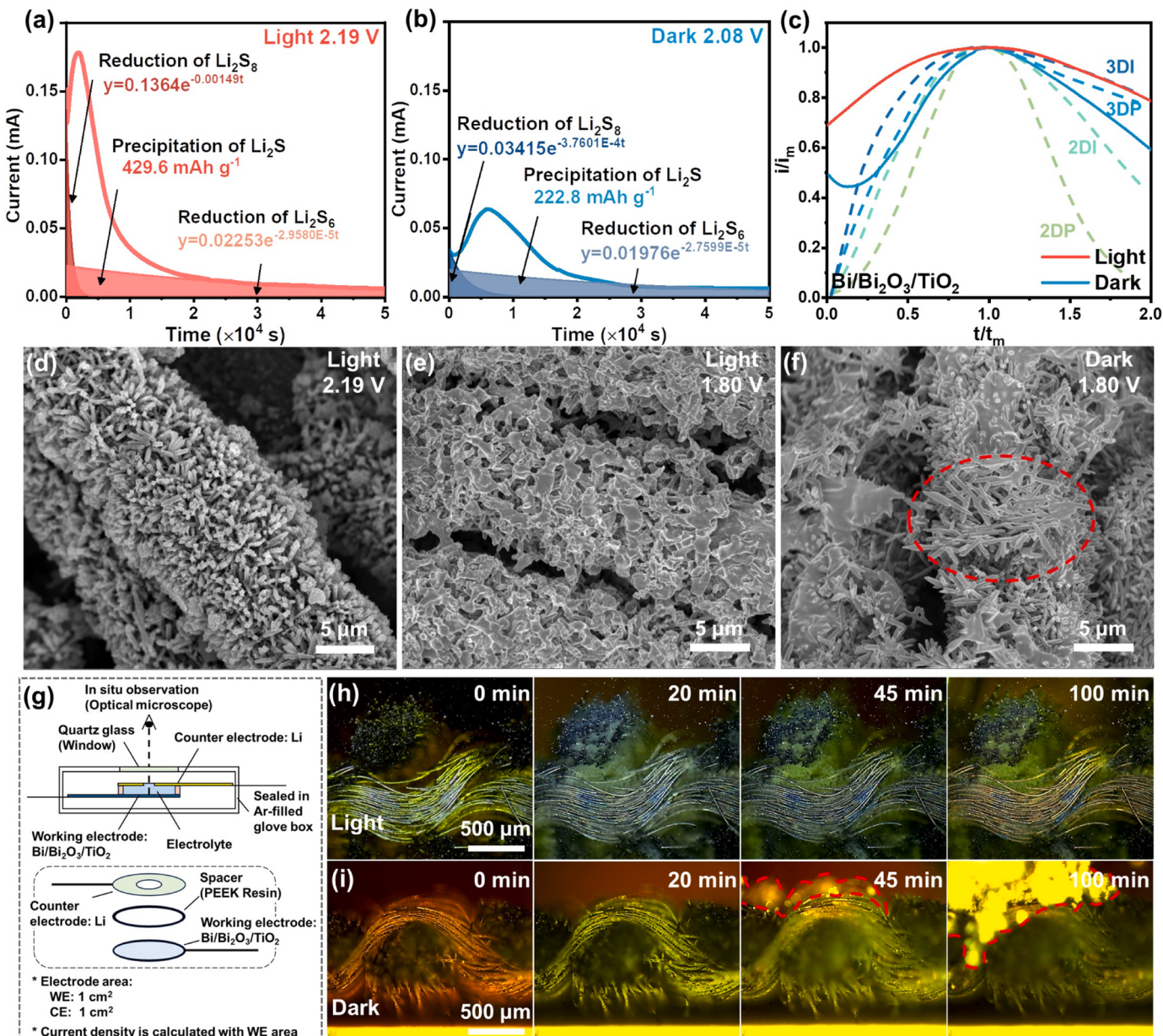


Fig. 5. Potentiostatic discharging curves of the Bi/Bi₂O₃/TiO₂ VPLSBs (a) with and (b) without visible light. (c) The dimensionless transient plots of Li₂S₈ deposition with and without visible light in Bi/Bi₂O₃/TiO₂ VPLSBs. SEM images of the Li₂S depositing on Bi/Bi₂O₃/TiO₂ under visible light at (d) 2.19 V, (e) 1.80 V, and (f) under dark at 1.80 V. (g) Schematic of an in-situ optical cell for optical microscopy. In-situ optical microscopy detection of the discharging process in the Bi/Bi₂O₃/TiO₂ photocathodes (h) with and (i) without visible light.

to track the dynamic Li₂S depositing process (Fig. 5g and Fig. S24). No significant change is observed on the electrode surface under light even after 100 minutes, while insoluble sediments start appearing at 45 minutes and rapidly grow to a thickness of 200 μm within 100 minutes under dark conditions (Fig. 5h-i and Movie S1-2). These findings provide compelling evidence for the substantial contribution of photocarriers, facilitated by the photoelectrocatalysis effect, in promoting the stability of the electrode interface.

The dynamic conversion of active substances in the Bi/Bi₂O₃/TiO₂ VPLSBs under visible light is comprehensively investigated using Raman spectroscopy and XPS characterizations. Samples are prepared under an Ar atmosphere, and stored in a vacuum chamber to prevent oxidation. Eight voltage features (1.7–2.8 V) are selected to represent the complete electrochemical cycle, as shown in Fig. 6a, under 0.06 W cm⁻² visible light. The presence of TiO₂ is confirmed by characteristic peaks at 240.5,

438.9, and 606.6 cm⁻¹ in Fig. 6b, while the absence of TiO₂^X signals near 920 cm⁻¹ demonstrates the chemical stability of TiO₂ (Fig. S25).[13] The remaining vibration bands at 152 cm⁻¹, 355 cm⁻¹, and 385 cm⁻¹ correspond to S₈, Li₂S, and polysulfides, as shown in the enlarged view in Fig. 6c. [11,12,42] Remarkably, in the fully discharged (point E) and recharged (point H) states, the polysulfide peak completely disappears, replaced solely by the presence of Li₂S or S₈, indicating the complete transformation of polysulfide species under light exposure. During discharge to 2.19 V at point C, the Li₂S peak at 355 cm⁻¹ indicates the photoelectrocatalytic reduction of polysulfide, promoting the nucleation of Li₂S. While recharging to 2.3 V at point F, the simultaneous appearance of S₈ and polysulfides bands indicates an efficient photoelectrocatalysis that synchronizes the conversion of Li₂S to polysulfide and the subsequent oxidation of polysulfide to S₈. The increased photoelectrocatalysis activity of the Bi/Bi₂O₃/TiO₂ photocathode under

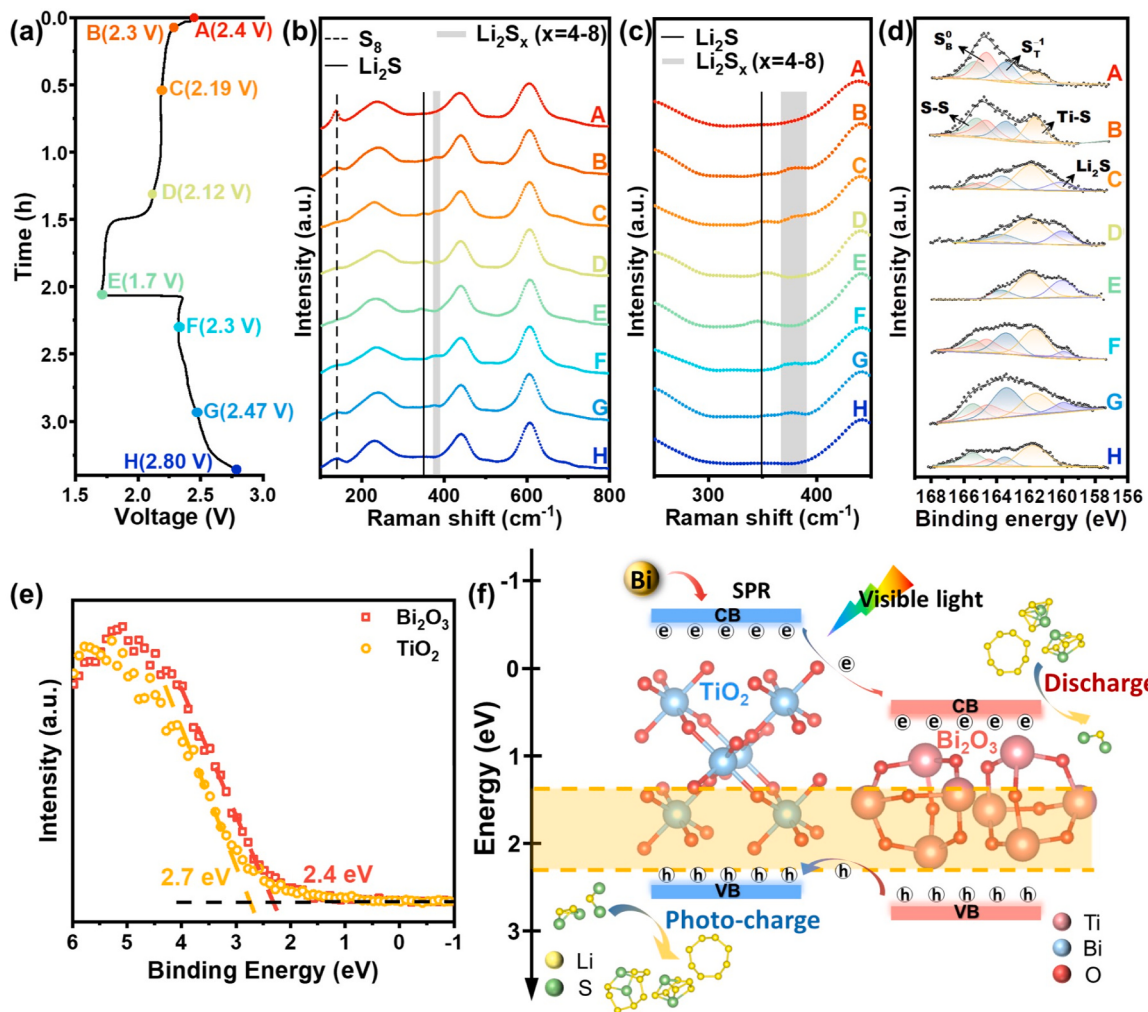


Fig. 6. (a) GDC curves of the Bi/Bi₂O₃/TiO₂ photocathode under visible light. Raman spectra of the Bi/Bi₂O₃/TiO₂ photocathode under visible light at circulating voltages in the range of (b) 100–800 cm⁻¹ and (c) 250–450 cm⁻¹. (d) Corresponding high-resolution XPS analysis of S 2p spectra of the Bi/Bi₂O₃/TiO₂ photocathode under visible light. (e) XPS valence band spectra of Bi₂O₃ and TiO₂. (f) Schematic illustration of the photogenerated carriers transfer and polysulfide conversion in the Bi/Bi₂O₃/TiO₂ photocathode.

visible light can be credited for the promoted sulfur species conversion and significantly shortened presence time of polysulfide intermediates.

XPS analysis is further employed to track the detailed evolution of sulfur species in the Bi/Bi₂O₃/TiO₂ VPLSBs, with a focus on the 2p_{3/2} segment of the high-resolution S 2p spectrum. The persistent Ti-S binding emission peak at 161.8 eV throughout the process in Fig. 6d suggests a favorable interaction between sulfur species and the Bi/Bi₂O₃/TiO₂ photocathode [34]. The presence of S₈ and Li₂S is confirmed by peaks at binding energies of 165.2 eV and 160 eV, while the doublet of peaks at 164.6 eV and 163.7 eV corresponds to bridging-S (S_B⁰) and terminal-S (S_T⁻¹), respectively [19,28,36]. During discharge reduction, the special transition from bridging-S to terminal-S is facilitated by reduced electron density below bridging-S bonds, reflecting a strong covalent interaction between Ti and S atoms due to abundant photocarrier generation near the cathode [23]. Noteworthy, the prevalence of terminal-S bonds provides abundant electrochemical active sites for higher electrocatalytic activity, while the evolution of bridging-S into metastable Li₂S_x (x > 4) would block pores, leading to reduced cell capacity and internal resistance [7,19]. These results show that the catalytic conversion activity of sulfur species can be improved under the photoelectrocatalysis effect of visible light, thus ensuring a continuous reversible redox process in the Bi/Bi₂O₃/TiO₂ VPLSBs.

The compatibility of energy levels between the Bi/Bi₂O₃/TiO₂

photocathode and the Li-S battery system is crucial for efficient photocarrier catalysis in polysulfide conversion, enabling effective electrochemical energy storage. The energy levels of the conduction-band (CB) bottom and valence-band (VB) maximum in rutile TiO₂ and Bi₂O₃, determined through density functional theory calculations, are −0.59/2.41 eV and 0.376 V/2.716 V vs. NHE, respectively (Fig. S26) [15,27,37–39]. These results are in agreement with the experimental measurements of VB XPS spectra, where the VB positions of Bi₂O₃ and TiO₂ are determined to be 2.4 and 2.7 eV vs. NHE (Fig. 6e). It is evident that the Bi/Bi₂O₃/TiO₂ energy band completely covers the Li-S redox range (1.9–2.3 V), confirming the matched energy levels between the photocathode and redox reactions (Fig. 6f) [24]. Distinguished from extensively studied Bi₂O₃/TiO₂ catalysts, the Bi/Bi₂O₃/TiO₂ electrode strategically underscores the unique role of metallic Bi, emphasizing its distinctive advantages such as bandgap adjustment, SPR effects, protective layers, and charge transfer bridges [16,32,37]. This approach accentuates the pivotal role of Bi in the system, followed by a parallel emphasis on the roles of Bi₂O₃ and TiO₂. Bi₂O₃ serves as the recipient and transmitter of transferred electrons and holes during the electron transfer process, while TiO₂ facilitates electron transfer, enabling SPR-excited electrons near Bi to transfer to the higher energy CB of Bi₂O₃. The synergistic roles of these components ensure a stable and abundant supply of photocarriers, facilitating efficient electrocatalysis of polysulfide conversion under visible light and achieving highly

effective light-to-electrical energy conversion and electrical-to-chemical energy storage in Bi/Bi₂O₃/TiO₂ VPLSBs. Such tailored separate pathways for electron and hole transfer, designed to match the Li-S redox potential range, ensure a stable and abundant supply of photocarriers with minimal recombination, thereby facilitating efficient electrocatalysis of polysulfide conversion under visible light. Leveraging the unique photoelectrocatalysis properties of the Bi/Bi₂O₃/TiO₂ photocathode, the highly efficient light-to-electrical energy conversion and effective electrical-to-chemical energy storage can be simultaneously achieved in the Bi/Bi₂O₃/TiO₂ VPLSBs [25].

In addition to photoelectrocatalysis capability, the Bi/Bi₂O₃/TiO₂ photocathode also exhibits photovoltaic property that plays a crucial role in the direct bare photo-charging process. This unique bare photo-charging process in the Bi/Bi₂O₃/TiO₂ VPLSB is further explored through a cycling experiment, involving a fully galvanostatic discharge, a ten-hour bare photo-charging without external voltage bias, and a complete galvanostatic discharge. In Fig. 7a, voltage exhibits a sudden increase upon each light contact from a fully discharged state, followed by a gradual rise over ten hours until reaching a stable equilibrium voltage of 2.3 V over long term. When exposed to higher light intensity (0.1 W cm⁻²), the Bi/Bi₂O₃/TiO₂ VPLSBs can reach a voltage of 2.35 V when fully charged, owing to more photogenerated carriers to overcome the internal polarization of the battery (Fig. S27). [4] Despite the constraint on open-circuit voltage (measured to be 2.35 V in Fig. S28, Supporting Information) due to electrode conduction band positions, the bandgap of the Bi/Bi₂O₃/TiO₂ electrode encompasses the redox reactions (1.7–2.3 V) inherent to the lithium-sulfur battery system, as depicted in Fig. 3h. As a result, the photo-light charging process remains effective in facilitating the reactions between Li₂S and polysulfide

intermediates (Fig. S29). The discharging voltage plateau at around 2.2 V shrinkage can be ascribed to the photocathode moderating cell polarization, accelerating internal reactions, and promoting complete polysulfide intermediates to Li₂S conversion. The subsequent bare photo-charging process exhibits remarkable stability lasting over 115 hours and consistently releasing photo-stored capacities, despite fluctuations in light intensity (Fig. 7b).

Over ten cycles of the bare photo-charging process, as depicted in Fig. 7c, the average additional discharging capacity can be measured at 464 mA h g⁻¹, representing 27.7 % of the theoretical specific capacity of typical Li-S batteries. Specifically, the visible light energy conversion and storage capability of the Bi/Bi₂O₃/TiO₂ VPLSBs is evaluated combined with the bare photo-charging current curves and bare photo-charging power curves (Fig. S30), offering valuable insights into their visible light absorption and utilization efficiency. Promisingly, the Bi/Bi₂O₃/TiO₂ VPLSBs exhibit an impressive overall visible light-to-chemical energy conversion efficiency of 2.58 % in Fig. 7d, surpassing state-of-the-art benchmarks for solar rechargeable batteries (Table S2). [2,5,41] While the average visible light-to-electrical energy photovoltaic conversion efficiency and the electrical-to-chemical energy storage efficiency of the Bi/Bi₂O₃/TiO₂ VPLSBs are 3.57 % and 77.2 %, respectively. The calculations details and results for ten cycles are concluded and listed in the Table S3. The efficient light-to-electrical energy conversion process in the Bi/Bi₂O₃/TiO₂ VPLSBs, driven by the photovoltaic effect, enables the direct incorporation of additional capacity into the battery system, resulting in enhanced battery performance in response to visible light.

The underlying mechanism of the direct light-to-electrical energy conversion in the Bi/Bi₂O₃/TiO₂ VPLSBs is analyzed, highlighting the

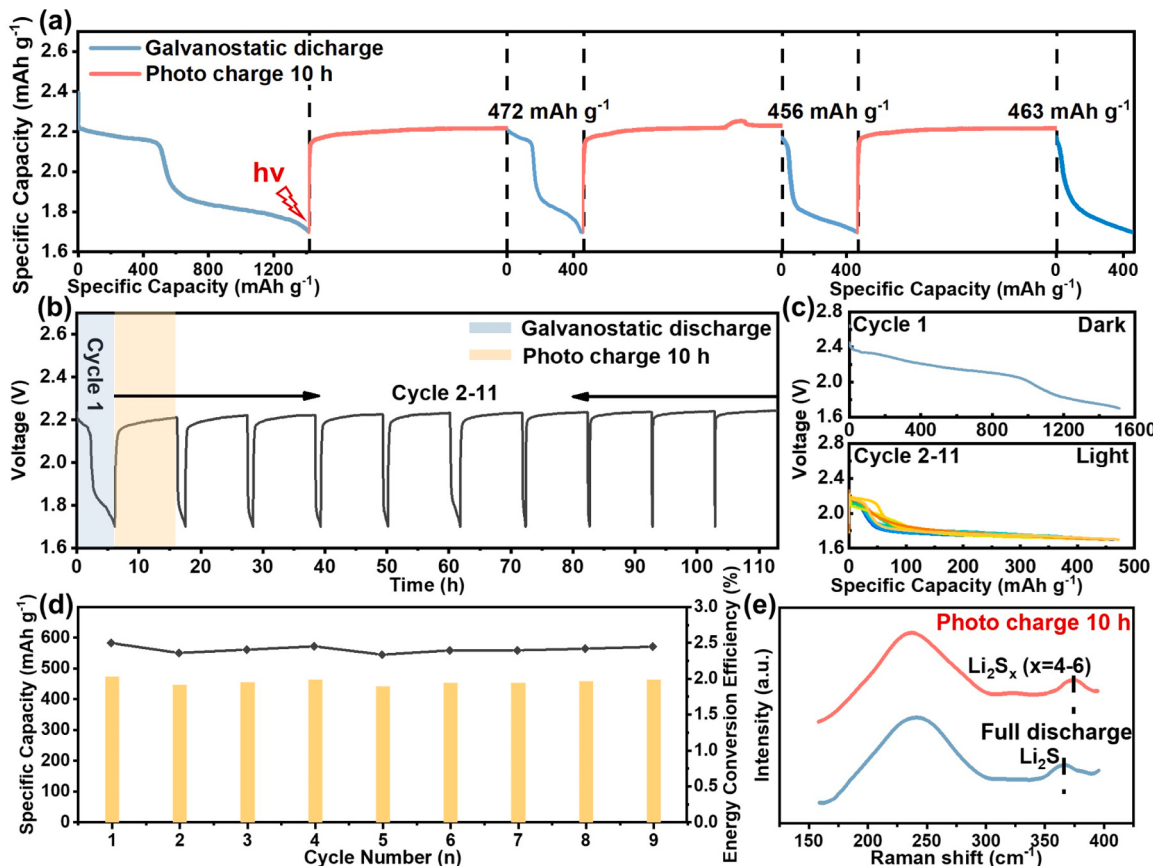


Fig. 7. (a) The bare photo-charging and galvanostatic discharging cycle tests with initial galvanostatic discharging, ten-hour bare photo-charging, and subsequent discharging steps. (b) Prolonged bare photo-charging and galvanostatic discharging curves and (c) capacity analysis for bare photo-charging in the Bi/Bi₂O₃/TiO₂ VPLSBs. (d) Energy conversion efficiencies of Bi/Bi₂O₃/TiO₂ VPLSB under ten-hour illumination. (e) Raman spectra analysis after full discharging and ten-hour bare photo-charging.

combined effects of the photovoltaic effect and photocatalytic reactions. Driven by photovoltaic effect, the Bi/Bi₂O₃/TiO₂ photocathode efficiently separates electrons from holes, allowing the direct injection of electrons into batteries via an external electron transport path. Moreover, the involvement of photocatalytic reactions is confirmed by the red-shift peak observed in Raman spectroscopy, indicating the conversion of Li₂S to Li₂S_x after bare photo-charging (Fig. 7e). Harnessing the power of light, the bare photo-charging process relies on the remarkable photoelectric activity of the material and the precisely designed band structure, creating a synergistic effect that matches the redox potential of the lithium-sulfur battery system. This breakthrough in direct light-to-electrical energy conversion revolutionizes battery performance, offering longer use time, and higher energy storage density, and opening new possibilities for sustainable energy storage applications.

4. Conclusions

We present the development of visible-light-driven photoelectrochemical Li₂S₆-based Li-S batteries that enable efficient light-electrical-chemical energy conversion and storage. This advancement is achieved through the use of light-permeable devices and a deliberately designed bifunctional Bi/Bi₂O₃/TiO₂ cathode, which serves as both a light harvester and redox catalyst, allowing simultaneous energy conversion and storage. The Bi/Bi₂O₃/TiO₂ heterostructure exhibits a narrower bandgap and well-matched energy levels with Li-S redox potentials, enhancing light harvesting and improving polysulfide conversion. The unique design of the Bi/Bi₂O₃/TiO₂ photocathode not only provides high stability by suppressing the shuttle effect in traditional lithium-sulfur batteries but also contributes additional energy through the bare photo-charging process. Leveraging the photovoltaic effect, the Bi/Bi₂O₃/TiO₂ VPLSBs demonstrate a remarkable photo-charging stored capacity of 458.9 mA h g⁻¹ with an impressive overall conversion-storage efficiency of 2.58 %. Furthermore, the VPLSBs exhibit a stable reversible capacity of 1484 mA h g⁻¹ and a Coulombic efficiency of 100.2 % during 900 cycles at 0.2 mA cm⁻² under visible light. This integrated design of VPLSBs opens new avenues for the development of high-efficiency light-electrical-chemical energy storage strategies, emphasizing the importance of advancing the development of more efficient light-rechargeable materials.

CRediT authorship contribution statement

Donghui Long: Writing – review & editing, Validation, Supervision, Resources, Investigation, Funding acquisition, Conceptualization. **Bo Niu:** Supervision, Methodology, Investigation, Funding acquisition. **Shan Yi:** Writing – review & editing, Writing – original draft, Validation, Project administration, Methodology, Investigation, Formal analysis, Data curation, Conceptualization. **Zhe Su:** Methodology, Investigation, Data curation, Conceptualization. Wang Xiaowei: Validation, Conceptualization. **Yayun Zhang:** Software. Chen Hongli: Validation, Resources, Methodology, Investigation, Formal analysis, Data curation. **Zhiqiang Zhao:** Validation, Methodology, Investigation, Formal analysis, Data curation.

Declaration of Competing Interest

The authors declare that they have no known competing financial interests or personal relationships that could have appeared to influence the work reported in this paper.

Data availability

Data will be made available on request.

Acknowledgements

This work was supported by National Natural Science Foundation of China (No. 22078100, No. 52102098, and No. 22008073) and Fundamental Research Funds for the Central Universities (No. 222201718002).

Appendix A. Supporting information

Supplementary data associated with this article can be found in the online version at doi:10.1016/j.apcatb.2024.123853.

References

- [1] P.E. Blöchl, Projector augmented-wave method, *PhRvB* 50 (24) (1994) 17953–17979, <https://doi.org/10.1103/PhysRevB.50.17953>.
- [2] Buddha Deka Boruah, Angus Mathieson, Bo Wen, Sascha Feldmann, Wesley M. Dose, Michael De Volder, Photo-rechargeable zinc-ion batteries, *Energy Environ. Sci.* 13 (8) (2020) 2414–2421, <https://doi.org/10.1039/d0ee01392g>.
- [3] P. Chen, G.R. Li, T.T. Li, X.P. Gao, Solar-driven rechargeable lithium-sulfur battery, *Adv. Sci. (Weinh.)* 6 (15) (2019) 1900620, <https://doi.org/10.1002/advs.201900620>.
- [4] Qian Cheng, Tianwei Jin, Yupeng Miao, Zhe Liu, James Borovilas, Hanrui Zhang, Shuwei Liu, So-Yeon Kim, Ruiwen Zhang, Haozhen Wang, Xi Chen, Long-Qing Chen, Ji Li, Wei Min, Yuan Yang, stabilizing lithium plating in polymer electrolytes by concentration-polarization-induced phase transformation, *Joule* 6 (10) (2022) 2372–2389, <https://doi.org/10.1016/j.joule.2022.08.001>.
- [5] Buddha Deka Boruah, Angus Mathieson, Sul Ki Park, Xiao Zhang, Bo Wen, Lifu Tan, Adam Boies, Michael De Volder, Vanadium dioxide cathodes for high-rate photo-rechargeable zinc-ion batteries, *Adv. Energy Mater.* 11 (13) (2021), <https://doi.org/10.1002/aenm.202100115>.
- [6] Qianwen Dong, Meng Wei, Qiuman Zhang, Lifeng Xiao, Xin Cai, Shengsen Zhang, Qiongzhii Gao, Yueping Fang, Feng Peng, Siyuan Yang, Photoassisted Li-ion deintercalation and Ni⁺/valence conversion win-win boost energy storage performance in Ni/Cds@Ni3s2-based li-ion battery, *Chem. Eng. J.* 459 (2023), <https://doi.org/10.1016/j.cej.2023.141542>.
- [7] Yuru Dong, Zhengju Zhu, Yanjie Hu, Guanjie He, Yue Sun, Qilin Cheng, Ivan P. Parkin, Hao Jiang, Supersaturated bridge-sulfur and vanadium Co-Doped MoS₂ nanosheet arrays with enhanced sodium storage capability, *Nano Res.* 14 (1) (2020) 74–80, <https://doi.org/10.1007/s12274-020-3044-x>.
- [8] H. Fan, H. Li, B. Liu, Y. Lu, T. Xie, D. Wang, Photoinduced charge transfer properties and photocatalytic activity in Bi2O3/Batio3 composite photocatalyst, *ACS Appl. Mater. Interfaces* 4 (9) (2012) 4853–4857, <https://doi.org/10.1021/am301199w>.
- [9] H. Fang, C. Battaglia, C. Carraro, S. Nemsak, B. Ozdol, J.S. Kang, H.A. Bechtel, S. B. Desai, F. Kronast, A.A. Unal, G. Conti, C. Conlon, G.K. Palsson, M.C. Martin, A. M. Minor, C.S. Fadley, E. Yablonovitch, R. Maboudian, A. Javey, Strong Interlayer Coupling in Van Der Waals heterostructures built from single-layer chalcogenides, *Proc. Natl. Acad. Sci. USA* 111 (17) (2014) 6198–6202, <https://doi.org/10.1073/pnas.1405435111>.
- [10] A. Gouder, F. Podjaski, A. Jimenez-Solano, J. Kroger, Y. Wang, B.V. Lotsch, An integrated solar battery based on a charge storing 2d carbon nitride, *Energy Environ. Sci.* 16 (4) (2023) 1520–1530, <https://doi.org/10.1039/d2ee03409c>.
- [11] M. Hagen, P. Schiffels, M. Hammer, S. Dörfler, J. Tübke, M.J. Hoffmann, H. Althues, S. Kaskel, In-Situ Raman investigation of polysulfide formation in Li-S cells, *J. Electrochem. Soc.* 160 (8) (2013) A1205–A1214, <https://doi.org/10.1149/2.045308jes>.
- [12] Julien Hannauer, Johan Scheers, Julien Fullenwarth, Bernard Fraisse, Lorenzo Stievano, Patrik Johansson, The quest for polysulfides in lithium-sulfur battery electrolytes: an operando confocal raman spectroscopy study, *ChemPhysChem* 16 (13) (2015), <https://doi.org/10.1002/cphc.201500708>.
- [13] Hu, Chen, Ling Chen, Yanjie Hu, Aiping Chen, Long Chen, Hao Jiang, and Chunzhong Li. Light-Motivated SnO₂/TiO₂ Heterojunctions Enabling the Breakthrough in Energy Density for Lithium-Ion Batteries. <https://doi.org/10.1002/adma.202103558>. Accessed 2023/03/23. <https://dx.doi.org/https://doi.org/10.1002/adma.202103558>.
- [14] Yuxiang Hu, Yang Bai, Bin Luo, Songcan Wang, Han Hu, Peng Chen, Miaoqiang Lyu, Joe Shapter, Alan Rowan, Lianzhou Wang, A portable and efficient solar-rechargeable battery with ultrafast photo-charge/discharge rate, *Adv. Energy Mater.* 9 (28) (2019), <https://doi.org/10.1002/aenm.201900872>.
- [15] Akio Ishikawa, Tsuyoshi Takata, Junko N. Kondo, Michikazu Hara, Hisayoshi Kobayashi, Kazunari Domen, oxy sulfide Sm₂ti₂s₂o₅ as a stable photocatalyst for water oxidation and reduction under visible light irradiation ($\lambda \leq 650$ nm), *J. Am. Chem. Soc.* 124 (45) (2002) 13547–13553, <https://doi.org/10.1021/ja0269643>.
- [16] Zhengbo Jiao, Mingdong Shang, Jiamei Liu, Gongxuan Lu, Xuesen Wang, Yingpu Bi, The charge transfer mechanism of Bi modified TiO₂ nanotube arrays: TiO₂ serving as a “charge-transfer-bridge”, *Nano Energy* 31 (2017) 96–104, <https://doi.org/10.1016/j.nanoen.2016.11.026>.
- [17] B. Kang, G. Ceder, Battery materials for ultrafast charging and discharging, *Nature* 458 (7235) (2009) 190–193, <https://doi.org/10.1038/nature07853>.

- [18] G. Kresse, J. Furthmüller, Efficient iterative schemes for ab initio total-energy calculations using a plane-wave basis set, *PhRvB* 54 (16) (1996) 11169–11186, <https://doi.org/10.1103/PhysRevB.54.11169>.
- [19] Matthew J. Lacey, Anurag Yalamanchili, Julia Maibach, Carl Tengstedt, Kristina Edström, Daniel Brandell, The Li-S battery: an investigation of redox shuttle and self-discharge behaviour with LiNO_3 -containing electrolytes, *RSC Adv.* 6 (5) (2016) 3632–3641, <https://doi.org/10.1039/c5ra23635e>.
- [20] G. Li, S. Wang, Y. Zhang, M. Li, Z. Chen, J. Lu, Revisiting the role of polysulfides in lithium-sulfur batteries, *Adv. Mater.* 30 (22) (2018) e1705590, <https://doi.org/10.1002/adma.201705590>.
- [21] N. Li, Y. Wang, D. Tang, H. Zhou, Integrating a photocatalyst into a hybrid lithium-sulfur battery for direct storage of solar energy, *Angew. Chem. Int. Ed. Engl.* 54 (32) (2015) 9271–9274, <https://doi.org/10.1002/anie.201503425>.
- [22] Tao Li, Umair Gulzar Xue Bai, Claudio Capiglia Yu-Jun Bai, Xufeng Zhou Wei Deng, Zhifu Feng Zhaoping Liu, Remo Proietti Zaccaria, A Comprehensive understanding of lithium-sulfur battery technology, *Adv. Funct. Mater.* 29 (32) (2019), <https://doi.org/10.1002/adfm.201901730>.
- [23] Yuanchang Li, Wenda Li, Xiujuan Yan, Zhenfang Zhou, Xiaosong Guo, Jing Liu, Changming Mao, Zhonghua Zhang, Guicun Li, Terminal Sulfur Atoms Formation Via Defect Engineering Strategy to Promote the Conversion of Lithium Polysulfides, *J. Mater. Sci. Technol.* 103 (2022) 221–231, <https://doi.org/10.1016/j.jmst.2021.06.050>.
- [24] Yu-Hao Liu, Wei Chang Jin Qu, Hong-Jun Liu Cheng-Ye Yang, Yu. Kang Xian-Zhi Zhai, Yu-Guo Guo, Zhong-Zhen Yu, A photo-assisted reversible lithium-sulfur battery, *Energy Storage Mater.* 50 (2022) 334–343, <https://doi.org/10.1016/j.ensm.2022.05.030>.
- [25] Liu, Yuhao, Xinlong Zheng, Yingjie Yang, Jing Li, Weifeng Liu, Yijun Shen, and Xinlong Tian. Photocatalytic Hydrogen Evolution Using Ternary-Metal-Sulfide/TiO₂.
- [26] Heterojunction Photocatalysts. *ChemCatChem* 14, no. 5 (2021). [https://doi.org/10.1002/cctc.202101439..](https://doi.org/10.1002/cctc.202101439)
- [27] J. Lv, J. Xie, A.G.A. Mohamed, X. Zhang, Y. Wang, Photoelectrochemical energy storage materials: design principles and functional devices towards direct solar to electrochemical energy storage, *Chem. Soc. Rev.* 51 (4) (2022) 1511–1528, <https://doi.org/10.1039/d1cs00859e>.
- [28] Vikash Mishra, M.Kamal Warshi, Aanchal Sati, Anil Kumar, Vinayak Mishra, Rajesh Kumar, P.R. Sagdeo, Investigation of Temperature-Dependent Optical Properties of TiO₂ Using Diffuse Reflectance Spectroscopy, *SN Appl. Sci.* 1 (3) (2019), <https://doi.org/10.1007/s42452-019-0253-6>.
- [29] Q. Pang, D. Kundu, M. Cuisinier, L.F. Nazar, Surface-enhanced redox chemistry of polysulfides on a metallic and polar host for lithium-sulphur batteries, *Nat. Commun.* 5 (2014) 4759, <https://doi.org/10.1038/ncomms5759>.
- [30] John P. Perdew, Kieron Burke, Matthias Ernzerhof, Generalized gradient approximation made simple, *Phys. Rev. Lett.* 77 (18) (1996) 3865–3868, <https://doi.org/10.1103/PhysRevLett.77.3865>.
- [31] John P. Perdew, J.A. Chevary, S.H. Vosko, Koblar A. Jackson, Mark R. Pederson, D. J. Singh, Carlos Fiolhais, Atoms, Molecules, solids, and surfaces: applications of the generalized gradient approximation for exchange and correlation, *PhRvB* 46 (11) (1992) 6671–6687, <https://doi.org/10.1103/PhysRevB.46.6671>.
- [32] Benjamin Scharifker, Graham Hills, Theoretical and experimental studies of multiple nucleation, *Electrochim. Acta* 28 (7) (1983) 879–889, [https://doi.org/10.1016/0013-4686\(83\)85163-9](https://doi.org/10.1016/0013-4686(83)85163-9).
- [33] Q. Shi, Y. Zhang, D. Sun, S. Zhang, T. Tang, X. Zhang, S. Cao, Bi(2)O(3)-Sensitized TiO(2) hollow photocatalyst drives the efficient removal of tetracyclines under visible light, *Inorg. Chem.* 59 (24) (2020) 18131–18140, <https://doi.org/10.1021/acs.inorgchem.0c02598>.
- [34] Yan-Xi Tan, Xiang Zhang, Jing Lin, Yaobing Wang, A perspective on photoelectrochemical storage materials for coupled solar batteries, *Energy Environ. Sci.* 16 (6) (2023) 2432–2447, <https://doi.org/10.1039/d3ee00461a>.
- [35] X. Tao, J. Wang, Z. Ying, Q. Cai, G. Zheng, Y. Gan, H. Huang, Y. Xia, C. Liang, W. Zhang, Y. Cui, Strong sulfur binding with conducting magneli-phase Ti(N)O₂ (N-1) nanomaterials for improving lithium-sulfur batteries, *Nano Lett.* 14 (9) (2014) 5288–5294, <https://doi.org/10.1021/nl502331f>.
- [36] J. Wang, E. Kim, D.P. Kumar, A.P. Rangappa, Y. Kim, Y. Zhang, T.K. Kim, Highly durable and fully dispersed cobalt diatomic site catalysts for Co(2) Photoreduction to Ch(4), *Feb 1, Angew. Chem. Int Ed. Engl.* 61 (6) (2022) e202113044, <https://doi.org/10.1002/anie.202113044>.
- [37] Q. Wu, Z. Yao, X. Zhou, J. Xu, F. Cao, C. Li, Built-in catalysis in confined nanoreactors for high-loading Li-S batteries, *ACS Nano* 14 (3) (2020) 3365–3377, <https://doi.org/10.1021/acsnano.9b09231>.
- [38] Jun Xiao, Weiyi Yang, Qi Li, Bi Quantum Dots on Rutile TiO₂ as Hole trapping centers for efficient photocatalytic bromate reduction under visible light illumination, *Appl. Catal. B: Environ.* 218 (2017) 111–118, <https://doi.org/10.1016/j.apcatb.2017.03.084>.
- [39] Kesong Yang, Ying Dai, Baibiaow Huang, Myung-Hwan Whangbo, Density functional characterization of the band edges, the band gap states, and the preferred doping sites of halogen-doped TiO₂, *Chem. Mater.* 20 (20) (2008) 6528–6534, <https://doi.org/10.1021/cm801741m>.
- [40] W.N. Zhao, S.C. Zhu, Y.F. Li, Z.P. Liu, Three-phase junction for modulating electron-hole migration in anatase-rutile photocatalysts, *Chem. Sci.* 6 (6) (2015) 3483–3494, <https://doi.org/10.1039/c5sc00621j>.
- [41] G. Zhou, H. Tian, Y. Jin, X. Tao, B. Liu, R. Zhang, Z.W. Seh, D. Zhuo, Y. Liu, J. Sun, J. Zhao, C. Zu, D.S. Wu, Q. Zhang, Y. Cui, Catalytic oxidation of Li₂s on the surface of metal sulfides for Li-S batteries, *Proc. Natl. Acad. Sci. USA* 114 (5) (2017) 840–845, <https://doi.org/10.1073/pnas.1615837114>.
- [42] Y. Zhou, S. Zhang, Y. Ding, L. Zhang, C. Zhang, X. Zhang, Y. Zhao, G. Yu, Efficient solar energy harvesting and storage through a robust photocatalyst driving reversible redox reactions, *Adv. Mater.* 30 (31) (2018) e1802294, <https://doi.org/10.1002/adma.201802294>.